

The Tsunamis Generated by the Hunga Tonga-Hunga Ha'apai Volcano on January 15, 2022

Patrick Lynett (✉ plynett@usc.edu)

Univ of Southern California <https://orcid.org/0000-0002-2856-9405>

Physical Sciences - Article

Keywords:

Posted Date: March 16th, 2022

DOI: <https://doi.org/10.21203/rs.3.rs-1377508/v1>

License:  This work is licensed under a Creative Commons Attribution 4.0 International License.

[Read Full License](#)

Version of Record: A version of this preprint was published at Nature on August 8th, 2022. See the published version at <https://doi.org/10.1038/s41586-022-05170-6>.

1 **The Tsunamis Generated by the Hunga Tonga-Hunga Ha'apai Volcano on January 15,**
2 **2022**

3

4 Patrick Lynett, Tsunami Research Center, University of Southern California, USA
5 [corresponding author, plynett@usc.edu]

6 Maile McCann, Tsunami Research Center, University of Southern California, USA

7 Zili Zhou, Tsunami Research Center, University of Southern California, USA

8 Willington Renteria, Tsunami Research Center, University of Southern California, USA

9 Jose Borrero, eCoast Marine Consulting and Research, Raglan, New Zealand, Tsunami Research
10 Center, University of Southern California, USA

11 Dougal Greer, eCoast Marine Consulting and Research, Raglan, New Zealand

12 'Ofa Fa'anunu, Tonga Meteorological Service, Tonga

13 Cyprien Bosserelle, New Zealand National Institute of Water and Atmosphere, Christchurch,
14 New Zealand

15 Bruce Jaffe, United States Geological Survey, USA

16 SeanPaul La Selle, United States Geological Survey, USA

17 Andrew Ritchie, United States Geological Survey, USA

18 Alexander Snyder, United States Geological Survey, USA

19 Brandon Nasr, United States Geological Survey, USA

20 Jaqueline Bott, California Geological Survey, USA

21 Nicholas Graehl, California Geological Survey, USA

22 Costas Synolakis, Tsunami Research Center, University of Southern California, USA

23 Behzad Ebrahimi, Tsunami Research Center, University of Southern California, USA

24 Ezgi Cinar, Tsunami Research Center, University of Southern California, USA

25 **Abstract**

26 On the evening of 15 January 2022 at approximately 5:15 pm local time (04:15 am UTC), the
27 Hunga Tonga-Hunga Ha'apai volcano unleashed a violent underwater eruption, blanketing the
28 surrounding land masses in ash and debris [1]. The eruption generated tsunamis observed
29 throughout the globe. An event of this type last occurred in 1883, during the eruption of Krakatau
30 [2], and thus here we have the first observations of a tsunami from a large emergent volcanic
31 eruption captured with modern instrumentation. The mechanisms of tsunami generation are rare
32 and complex, but a wealth of observations permit a forensic analysis. Using oceanographic and
33 meteorological data, post-event field survey observations, and high-order hydrodynamic
34 modeling, we show that the event generated tsunamis at different times and from distinct
35 mechanisms. The main eruption appears to have generated waves through multiple mechanisms,
36 including: 1) air-sea coupling with the initial and powerful shockwave radiating out from the
37 explosion in the immediate vicinity of the eruption, 2) the collapse of the water-crater created by
38 the underwater explosion, and 3) air-sea coupling with the air-pressure pulse that circled the earth
39 multiple times, leading to a global tsunami. In the nearfield, the tsunami impacts are strongly
40 controlled by the water-crater source, while the far-field tsunami, which was uncommonly
41 persistent, can be largely described by the air-pressure pulse mechanism. Catastrophic damage in
42 some harbors in the far-field was averted by just tens of centimeters, implying that a modest sea
43 level rise combined with a future, similar event would lead to a step-function increase in
44 infrastructure impacts. Piecing together the complexity of this event has broad implications to the
45 hazard in similar geophysical settings, potentially indicating a currently neglected source of global
46 tsunamis.

47

48 **Main**

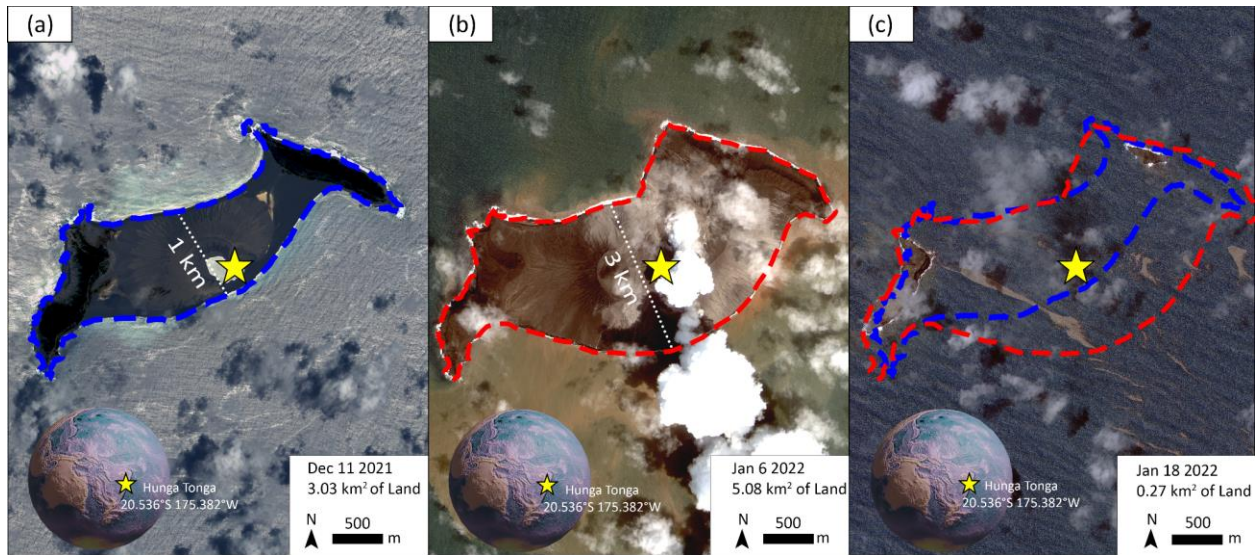
49 The archipelago of Tonga consists of a semi-continuous chain of 169 islands covering a span of
50 800 km north to south. The Tongan islands lie within the Tonga-Kermadec Ridge, the submarine
51 mountain range that contains the most seismically active subduction boundary on earth, thus
52 sustaining a high rate of submarine volcanoes [3]. The Hunga Tonga-Hunga Ha'apai volcano
53 (herein stated as Hunga Tonga) is one of a number of active volcanoes in the area and began an
54 active phase in late 2021. Due to intermittent eruptions from 29 December 2021 to 4 January 2022,
55 the emergent land area at Hunga Tonga increased from 3.03 km² to 5.08 km², as pictured in Fig.1
56 (a)-(b). After multiple days of significantly decreased activity, the submarine volcano had an
57 intense, explosive eruption on 15 January 2022 at 04:15 UTC [1]. Previous land areas vanished,
58 leaving behind two small islands above the sea. Satellite photos demonstrating the dramatic
59 changes are shown in Fig.1 (b)-(c). The eruption generated a tsunami that was observed globally;
60 a phenomenon that was last observed 140 years ago.

61 On 27 August 1883, the Krakatau volcano in the Sunda Strait between Java and Sumatra produced
62 four explosive eruptions over 5 hours that unleashed a series of tsunami waves, causing the
63 destruction of hundreds of towns and villages and killing at least 36,000 people [4]. However, the
64 highest reported runup of 41 m is from Merak on the west coast of Java and does not reflect the
65 height of the tsunami at the source [5]. From the much smaller eruption and flank collapse of
66 Anak Krakatau in 2018, Borrero et. Al. (2020) recorded ~80 m tsunami runup at the volcano and
67 ~1 m at Merak, indicating that the 41 m runup observed at Merak in 1883 must have been
68 associated with a tsunami near Krakatau possibly hundreds of meters in height [6].

69 Sea level disturbances observed in the far-field were due to the coupling of the sea surface and
70 generated air-pressure pulses from the great explosion of Krakatau, which was the third of the four
71 eruptions [7]. The tsunami was recorded by notably distant tidal gauges, such as the gauge at the
72 Gulf of Aden 11,000 km away from the source. This gauge recorded a 13 cm tsunami 12 hours
73 after the explosion, an anomalous observation for such a distance from the eruption [8]. The
74 tsunamis generated by Krakatau in 1883 are a close analogy to those observed from the Hunga
75 Tonga eruption, albeit the former was more intense. Through analysis of instrumental data, post-
76 event surveys, and detailed hindcast modeling, we will show that the Hunga Tonga eruption likely
77 generated tsunamis through three different mechanisms occurring at no less than two distinct
78 times.

79 Eyewitness accounts in Tonga indicate an early wave arrived roughly ten minutes before the
80 primary tsunami. This is substantiated by a small signal on the Tonga tide gauge, which arrived
81 too early to be a product of the major eruption at 04:15 UTC. Thus, this precursor tsunami must
82 have been generated by an earlier eruption or a submarine landslide. This smaller event fortuitously
83 acted as an evacuation warning in Tongatapu, likely averting loss of life. Following the major
84 eruption, a series of tsunamis were observed throughout the Pacific. In this paper, we will discuss
85 the observations and impacts of this event, the source mechanisms of these waves, and our efforts
86 to resolve the mechanics of generation through numerical modeling.

87

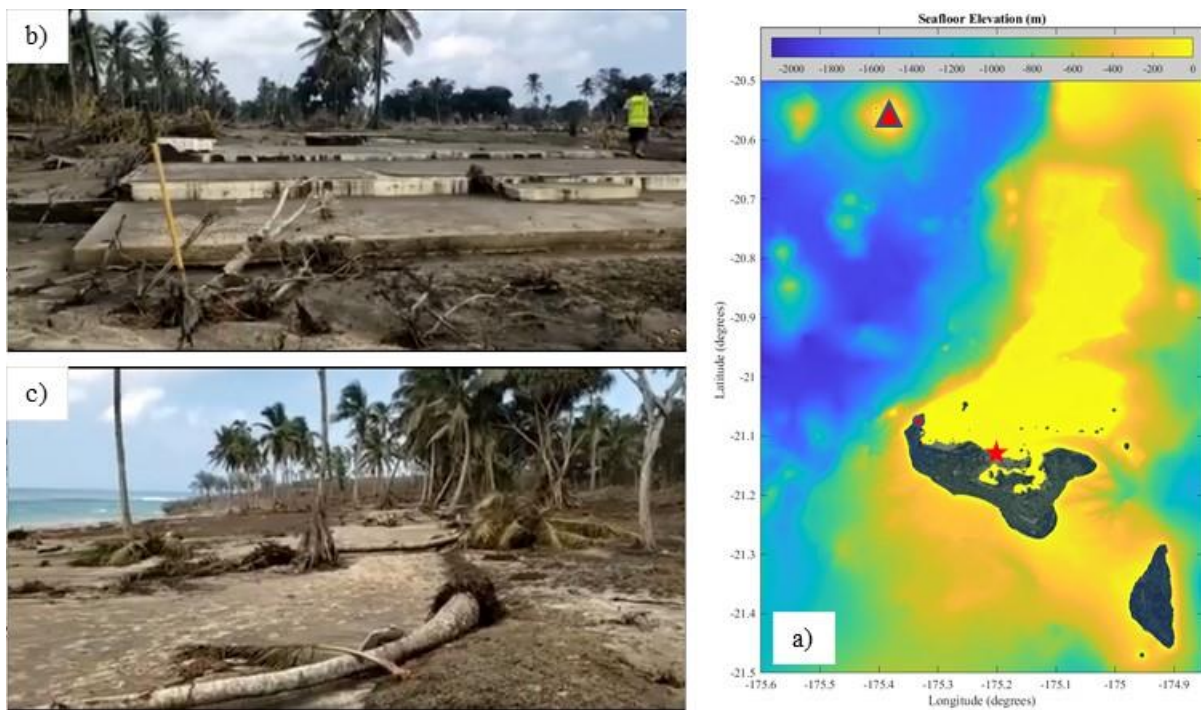


88
 89
 90 Fig.1 Satellite photos of Hunga Tonga taken on (a) 11 December 2021, (b) 6 January 2022, (c) 18
 91 January 2022 after the eruption. Original satellite imagery was sourced from UNOSAT [9]; global
 92 bathymetry data was sourced from GEBCO [10]. We calculated land area from the imagery using
 93 computer vision.

94 **Tsunami Observations and Impacts**

95 We will first discuss eyewitness accounts and observed impacts from the tsunami, starting from
 96 locations nearest to the source. Ongoing travel restrictions in Tonga associated with the COVID-
 97 19 pandemic have prevented researchers from obtaining direct measurements of the tsunami height
 98 or the extents of inundation. Therefore, we rely on eyewitness accounts and scant quantitative data.
 99 For example, we have evidence that a weather station positioned on a cell phone tower with base
 100 at a ground elevation of 13 m above sea level was destroyed by the tsunami in Kanokupolu, a town
 101 in western Tongatapu. The station observed the onset of the eruption and reported data until 6 pm
 102 local time (05:00 UTC). Three days after the tsunami, a site visit revealed that the tower had been
 103 toppled and transported approximately 20 m from its original location, indicating tsunami heights
 104 greater than 13 m above mean sea level.

105 Photos and video taken at a beach resort in Ha'atafu, also in western Tongatapu, demonstrate the
106 scale of the destruction in the nearfield. The resort, located at an estimated elevation of 5-10 m
107 above mean sea level, was completely destroyed. The built structures were reduced to foundations
108 and the original densely vegetated shoreline was stripped to bare earth (Fig. 2). Eyewitness reports
109 from Ha'atafu suggest that tsunami waves reached the resort prior to the residents hearing the
110 largest explosions from the erupting volcano. It was these early waves which prompted initial
111 evacuations, thus limiting casualties. At the Tongan capital of Nuku'alofa, located on the more
112 protected northern coast of Tongatapu, much smaller tsunami heights of less than 5 m were
113 observed.



114

115 Fig.2 Tsunami impacts on the island of Tongatapu. a) Locations of the volcano (red triangle), the
116 main islands of Tongatapu and 'Eua to the south, the photographs (red circle), and the Nuku'alofa
117 tide gauge (red star) overlaid on the seafloor elevation map; b) the foundation of a washed away
118 structure in Ha'atufa; c) beach front in Ha'atufa, previously lush with green vegetation.

119

120 New Zealand's array of Deep-ocean Assessment and Reporting of Tsunamis (DART) tsunameters
121 recorded tsunamis along the Tonga-Kermadec trench and to the west in the Coral Sea. From the
122 initial wave, the sensors recorded peak to trough (P2T) heights of approximately 35 cm and wave
123 periods of 10 to 40 minutes. Approximately 90 minutes later, the highest positive amplitude of just
124 over 20 cm was recorded during a burst of relatively short period (3-5 minute) waves (see Methods
125 for spectral analysis).

126 Coastal tide gauges around New Zealand, primarily in harbors, also clearly observed the tsunami.
127 However, the signal at some stations was complicated by the presence of storm waves due to ex-
128 tropical cyclone Cody which was simultaneously affecting the region. Measured tsunami
129 amplitudes ranged from 20 to 80 cm, with a peak amplitude of 1.3 m measured at Great Barrier
130 Island off Auckland's east coast. The small marina at Tutukaka on the northeast coast of New
131 Zealand is a well-known tsunami 'hotspot' [11] and incurred severe damage during this event. The
132 strong tsunami-induced currents entering and exiting the marina area through a narrow entrance
133 between two breakwaters caused damage to floating docks and tore vessels from their moorings,
134 leading to numerous collisions. Around New Zealand, bays and harbors prone to long wave
135 resonance were activated by the surges, with Wellington Harbor in particular showing a long-
136 lasting resonant signal at its fundamental modes [12, 13].

137 Moving to the distant far field, tsunami impacts were observed and recorded by the authors at
138 Ventura Harbor, CA, USA during the day on 15 January 2022. The leading crest of the air-pressure
139 pulse arrived in Ventura at 11:54 UTC (03:54 PST), or 7.65 hours after the explosion, and shortly
140 thereafter initial oscillations in the harbor were detected. Larger waves started to arrive near 15:30
141 UTC (07:30 PST), and the peak intensity of the waves and associated damage was observed in the
142 late morning to afternoon on 15 January. Throughout the next 30 hours, the tide gauge in the inner

143 harbor recorded continuous tsunami fluctuations of at least +/- 0.6 m, with the largest P2T heights
144 of 1.8 - 2.4 m.

145 Observations of currents exiting Ventura Harbor indicated that the speed increased as the tide
146 receded, peaking at approximately 21:00-23:00 UTC (13:00-15:00 PST), corresponding to lower
147 tidal elevations. Most of the damage to fixed infrastructure occurred at low tide (22:51 UTC), or
148 11 hours after the initial waves reached the harbor. At least three major docks were destroyed,
149 including a 27 m section of dock attached to four pilings, a commercial dock holding multiple
150 slips, and a 9 m residential dock. Additionally, a total of 23 residential floating dock ramps were
151 lifted from supports and carried out by the currents.

152 Further north in Santa Cruz Harbor, CA, USA, significant waves were first observed at 15:00 UTC
153 (07:00 PST). The seventh tsunami crest after this time was the largest, arriving near high tide at
154 16:50 UTC (08:50 PST). This surge flooded parking lots and damaged vehicles, docks, bathrooms,
155 dredging equipment, and other infrastructure around the harbor causing an estimated \$6.5 million
156 in damage [14]. This damage was mainly the result of flooding on-land facilities, which differs
157 from the in-water infrastructure impacts experienced in Ventura Harbor. However, during the
158 highest elevation tsunami crest, floating docks in the rear of Santa Cruz Harbor were less than 30
159 cm from the tops of the piles, indicating that a similar event at a slightly higher tide or sea level
160 would have led to widespread destruction in the harbor. Maximum tsunami runup at the harbor
161 and nearby beaches was estimated by well-preserved wrack lines of lightweight plant material and
162 wood, measured with survey-grade GPS receivers. At Santa Cruz Harbor, the highest runup was
163 3.97 m above Mean Lower Low Water (MLLW), which is 2.22 m above the predicted high tide
164 [15]. At beaches along Monterey Bay 10 and 13 km southeast of the harbor, tsunami runup markers
165 were surveyed at 3.71 m and 4.28 m above MLLW.

166 In South America, widespread tsunami amplitudes of approximately 1 m were observed. Some
167 coastal locations (Puerto Ayora, Ecuador; Callao, Peru; Arica, Chile; Coquimbo, Chile)
168 experienced persistent sea-level perturbations for more than 24 hours. According to Peru's
169 National Institute of Civil Defense, two people died due to the tsunami at Naylamp beach in the
170 Lambayeque District [16]. At Callao, Peru the first tsunami crest, likely generated by the air-
171 pressure pulse, arrived around 14:30 UTC; the main, hazardous waves arrived five hours later. In
172 the nearby La Pampilla oil terminal, the oil tanker vessel *Mare Doricum* reported the breaking of
173 mooring ropes, which caused an oil release of approximately 6,000 barrels. By international
174 standards, this is classified as a large oil spill [17].

175 **Pressure Observations**

176 In this event, tsunami generation occurs through two air-sea coupling stages. The first stage is
177 immediately after the eruption, when a high Mach number shockwave radiates away from the
178 explosive eruption. For an eruption energy in the range of 4-18 megatons of TNT (1.6×10^{16} -
179 7.5×10^{16} J) the shockwave would have traveled 2.9-4.8 km from the source before transitioning
180 from a supersonic shock to a sonic wave, with an initial Mach number greater than 6.0 and peak
181 explosive pressure greater than 3000 kPa [18]. Thus, for the Hunga Tonga eruption, the shockwave
182 to sonic wave transition would have occurred in just a few seconds following the eruption. The
183 sonic wave continued its propagation away from the volcano at the speed of sound, reaching
184 Tongatapu just over three minutes after the eruption.

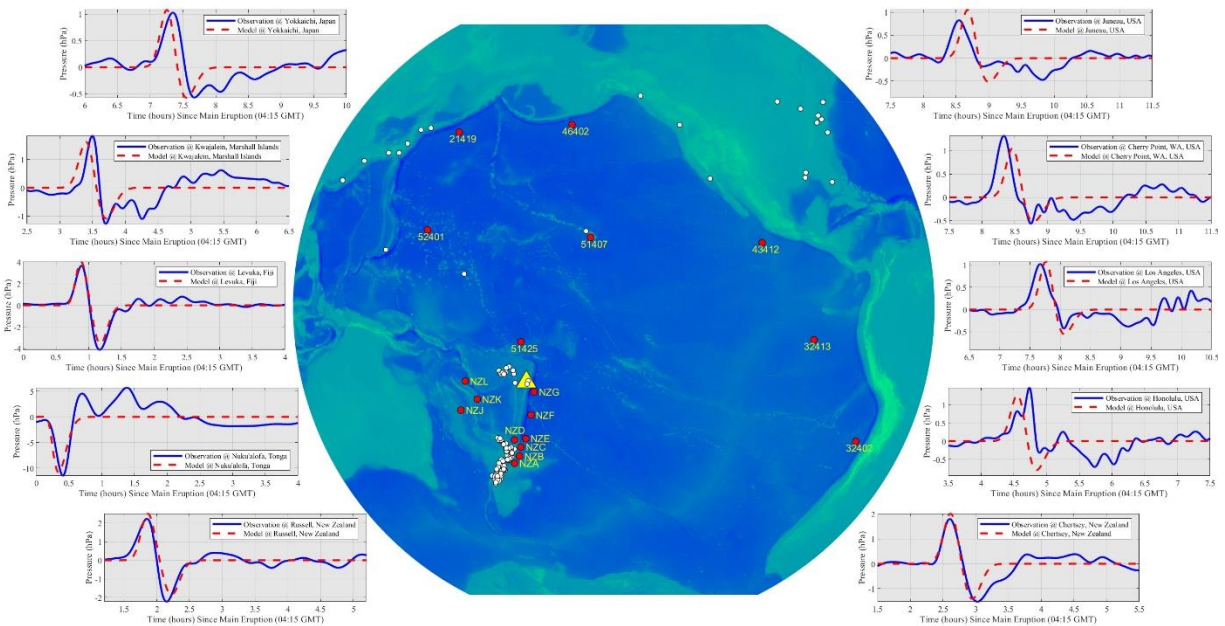
185 Through a complex process driven by explosion and shockwave generated pressure, temperature,
186 and density gradients, a stable acoustic wave (herein stated as the air-pressure pulse) radiates out
187 from the source through the atmosphere [19]. This wave forms into a leading positive-pressure

188 crest and a trailing negative-pressure trough, known as an “N-wave” [20]. This wave was captured
189 on weather station pressure sensors around the world, and is responsible for generating the far-
190 field tsunami observed throughout the Pacific. The moving pressure adds momentum to the ocean
191 surface through a pressure-gradient forcing that pushes the ocean surface in the direction of the
192 positive pressure gradient.

193 We developed a N-wave model for the evolution of the air-pressure pulse to recreate this tsunami
194 generation mechanism. We calibrated this model using observational data from 143 weather
195 stations throughout the Pacific, as summarized in Figure 3. The model accurately captures the
196 arrival time, amplitude, and shape of the air-pressure pulse, from the nearest pressure observation
197 in Tongatapu to far field locations in Japan and the USA. We emphasize that this model predicts
198 the air-pressure pulse and not the early-time shockwave.

199

200



201

202 Fig.3: Observed pressure signals in hPa (one hPa = 1 mb), throughout the Pacific used to calibrate
 203 the N-wave pressure pulse model, and the corresponding location of the station that recorded the
 204 signal. Red lines on each time series plot represent the model result; blue lines represent the
 205 measured pressure signal. Shown on this map are the 143 weather stations used to calibrate the
 206 pressure pulse model (white dots), the deep-sea DART sensors (red dots, with name labels), and
 207 the Hunga Tonga volcano (yellow triangle).

208

209 **Tsunami Modeling & Discussion**

210 Tsunamis were generated through three different mechanisms related to the explosive eruption at
 211 04:15 UTC: 1) air-sea coupling with the early-time shockwave, 2) waves generated by the
 212 equilibrium response to the water crater generated by the explosion, and 3) air-sea coupling with
 213 the global air-pressure pulse. We performed the tsunami simulation using a highly nonlinear
 214 dispersive water wave code [21], as described in the Methods section. We remark here that, due
 215 to the widespread and energetic 3-5-minute period energy observed in the DART tsunami data, the
 216 use of a dispersive model is necessary to properly capture the water wave propagation. Figure 4
 217 summarizes the simulation results and additional comparisons are provided in the Methods section.

218 The most challenging water level observation to explain is the measurement nearest to the source
219 – the tide gauge at Nuku’alofa, Tonga, approximately 65 km from the volcano. The shockwave
220 and crater source in our model can recreate the tide signal starting at 0.4 hours (~25 minutes) after
221 the eruption. It is physically impossible for water wave to arrive at the tide station earlier than this
222 if generated by the primary explosive eruption. However, the tide station data at Nuku’alofa
223 indicates a series of relatively small amplitude waves arriving just 10 minutes after the eruption.
224 These early waves would have arrived on the western facing beaches of northwest Tongatapu
225 immediately *before or during* the 04:15 UTC eruption and 3-4-minutes before residents would
226 have heard the sound of the explosion, which is consistent with the eyewitness accounts at this
227 location. Thus, we can confidently state that there was a small tsunami source prior to the main
228 eruption. While the available water level data for this precursor tsunami is too limited to precisely
229 describe the source, it is plausible the tsunami was generated by an earlier minor eruption and/or
230 a submarine landslide, which in turn may have destabilized the caldera and led to the explosive
231 eruption 10 minutes later.

232 Further from the volcano, the tsunami generated by the air-pressure pulse is significant in the
233 measured pressure signals. While the physics of the tsunami generated through a moving pressure
234 pulse are well understood [22], the wave field nonetheless becomes highly complex. Utilizing the
235 weather station observations, we calculate the time-averaged speed of the pressure crest to be 305
236 m/s at locations in the far field. The air-pressure pulse is moving faster than the tsunami can travel
237 in all depths less than 9.5 km. At a depth of 9.5 km, the speed of the pressure pulse and the speed
238 of the tsunami match, a phenomenon known as Proudman resonance [23] occurs, and the
239 amplitude of the tsunami grows rapidly. While the speed match represents the optimum conditions
240 to maximize the tsunami height, the amplitude of the tsunami generated by the air-pressure pulse

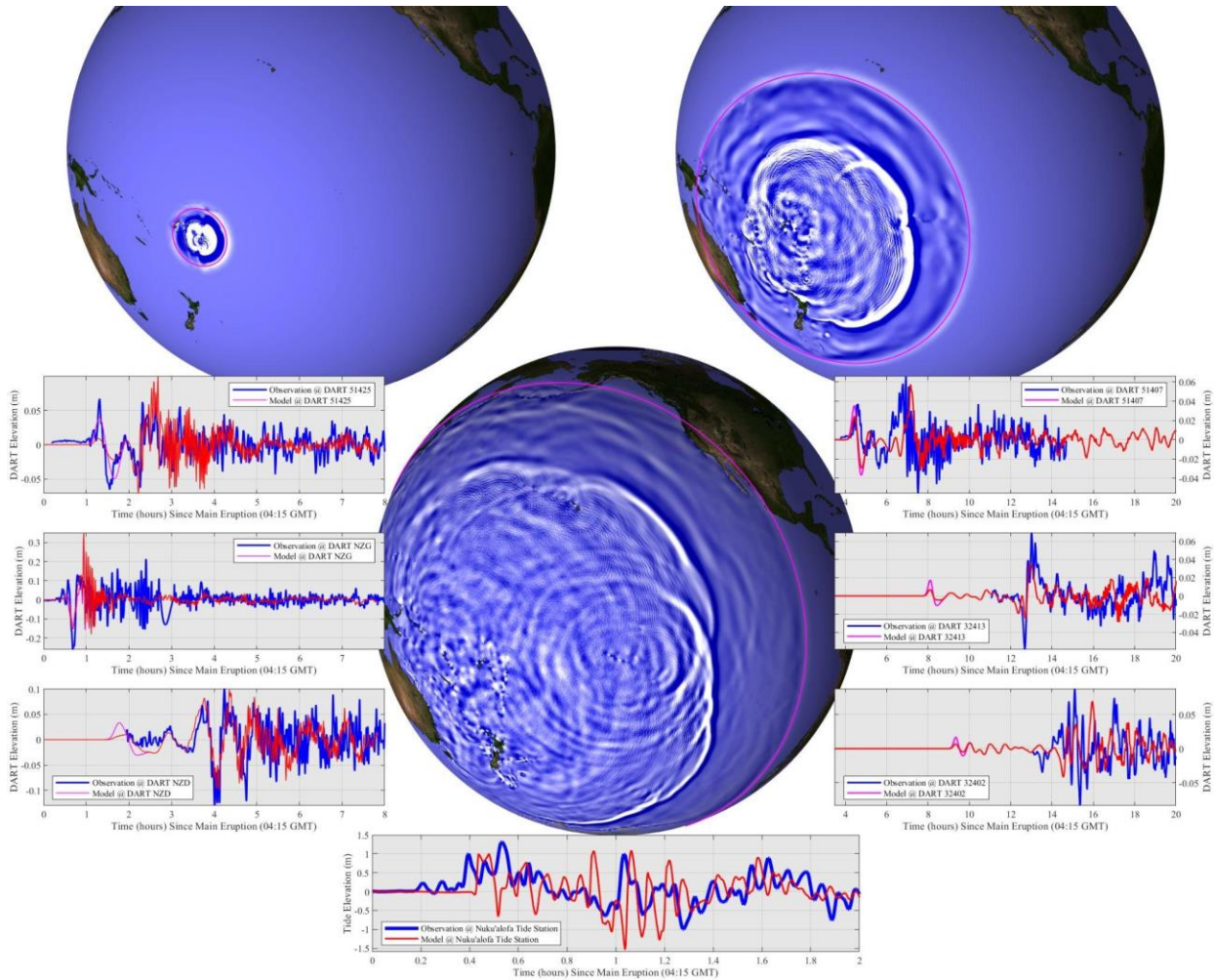
241 will increase as the speed match is approached. For example, the air-pressure pulse will create a
242 greater height tsunami in 5 km of water than in 1 km of water, even though Proudman resonance
243 is never reached. We clearly observe this effect during the Hunga Tonga eruption. As the air-
244 pressure pulse passes over the Tonga-Kermadec Trench, with widespread water depths in excess
245 of 9 km, the amplitude of the tsunami increases quickly, sending an energetic beam of energy
246 towards the Americas. The air-pressure pulse then outruns the tsunami it generated over the
247 Trench, leaves a slower-moving “free” gravity-wave tsunami behind, and continues to generate
248 small wave disturbances while passing over irregular bathymetry.

249 In the South Pacific, as observed by the DART stations NZD, NZG, and 51425 (Fig. 4), the tsunami
250 signal is clearly composed of a) the “pressure-forced” tsunami carried by the air-pressure pulse
251 arriving first, b) the “free” tsunami generated by the air-pressure pulse earlier in the event with
252 periods of 10-25 minutes, and c) short waves generated by the crater collapse and/or possibly other
253 complex sources at the volcano, with periods of 3-5 minutes. The tsunamis of b) and c) arrive tens
254 of minutes to hours after the tsunami of a). We note that for the tsunami associated with a), the
255 DART sensor, which is an ocean bottom pressure recorder, measures both the pressure from the
256 amplitude of the tsunami as well as the air pressure acting on it. This implies that during these
257 events, the type of water level sensor (i.e. bottom pressure sensor vs surface float or surface radar)
258 will yield different estimates of water level, as some will capture the air-pressure and some will
259 not.

260 In Hawaii (and DART station 51407), the air-pressure pulse arrives ~4.5 hours after the eruption,
261 followed by the main tsunami, composed primarily of waves generated earlier by the pressure
262 pulse when passing through the Central Pacific Basin, at 7 hours after the eruption. In the East
263 Pacific, the passing of the air-pressure pulse did not trigger the DART system to enter its high-

264 frequency sampling mode at stations 32413 and 32402. This mode did not activate until the larger
265 “free” tsunami, created as the pressure pulse passed over the Kermadec Trench, arrived 3-4 hours
266 later. A similar situation is found along the west coast of North America, where minor waves from
267 the passage of the pressure pulse are predicted and observed around 12:00 UTC, with larger waves
268 arriving hours later at 15:00 UTC. As the air-pressure pulse passes over the deep-water subduction
269 zone trenches throughout the Pacific, the Proudman resonance effect is activated, inducing a
270 phenomenon where every major trench in the Pacific basin effectively generates a small tsunami,
271 with crest length equal to the length of the trench. The result is tsunami energy generated from the
272 entire extent of the Pacific Rim over the course of 12 hours, leaving the Pacific Ocean filled with
273 tsunamis traveling in all directions, and causing the unique persistence of this event observed along
274 coastlines and harbors throughout the Pacific.

275



276

277 Fig.4: Summary of the simulation results from the highly nonlinear dispersive water wave model
 278 we utilize to recreate the three tsunamis generated by this event. The wave field in the Pacific is
 279 shown at three different times on the globes, at 1-hour post-eruption (05:15 UTC) in the upper left,
 280 4 hours post-eruption (08:15 UTC) in the upper right, and 8 hours post-eruption (12:15 UTC) in
 281 the lower middle. In each of these plots, the crest location of the pressure pulse is given by the
 282 magenta line; note how in the 12:15 UTC image the pressure pulse, crossing into North America,
 283 has far outrun the main tsunami it generated earlier, which at this time has just passed through
 284 Hawaii. Model-data comparisons are given in the time series plots at the Nuku'alofa tide station
 285 (lower plot, location given in Figure 2) and various DART stations (note locations given in Figure
 286 3). In the DART comparisons, the red line shows the modeled ocean surface elevation, while the
 287 magenta line provides the modeled ocean surface plus the pressure head from the pressure pulse.

288

289 **References**

290 [1] USGS. "M 5.8 Volcanic Eruption – 68 km NNW of Nuku'alofa, Tonga" .. 15 January 2022.
291 Archived from the original on 17 January 2022. Retrieved 15 January 2022.

292

293 [2] Self, S. & Rampino, M.R. The 1883 eruption of Krakatau. *Nature*. 294 (5843), 699-704
294 (1981).

295

296 [3] Schofield, J. C. Notes on the geology of the Tongan Islands. *New Zealand Journal of*
297 *Geology and Geophysics*. 10:6, 1424-1428 (1967).

298

299 [4] Sigurdsson, H., Houghton, B., McNutt, S., Rymer, H., & Stix, J. (Eds.). The encyclopedia of
300 volcanoes. Elsevier. (2015)

301

302 [5] Simkin, T., & Fiske, R. S. KRAKATAU 1883: A Centennial Retrospective on the Eruption
303 and its Atmospheric Effects. *Weatherwise*, 36(5), 244-254. (1983)

304

305 [6] Borrero, J. & Greer, S.D. Comparison of the 2010 Chile and 2010 Japan tsunamis in the Far-
306 field. *Pure and Applied Geophysics*, 170, 1249-1274. (2013).

307

308 [7] Pararas-Carayannis, G. Near and far-field effects of tsunamis generated by the paroxysmal
309 eruptions, explosions, caldera collapses and massive slope failures of the Krakatau volcano in
310 Indonesia on August 26-27, 1883. *Science of Tsunami Hazards*, 4, 191-201. (2003).

311

312 [8] Jordan, B.R. Tsunamis of the Arabian Peninsula a guide of historic events. *Science of*
313 *Tsunami Hazards*, 27, 31. (2008).

314

315 [9] UNITAR. *UNOSAT Emergency Mapping service activated over Tonga for the volcanic*
316 *eruption and induced tsunami*. [[https://unitar.org/about/news-stories/news/unosat-emergency-](https://unitar.org/about/news-stories/news/unosat-emergency-mapping-service-activated-over-tonga-volcanic-eruption-and-induced-tsunami)
317 [mapping-service-activated-over-tonga-volcanic-eruption-and-induced-tsunami](https://unitar.org/about/news-stories/news/unosat-emergency-mapping-service-activated-over-tonga-volcanic-eruption-and-induced-tsunami)] (United Nations
318 Institute for Training and Research, accessed 20 January 2022).

319

320 [10] GEBCO. *Gridded Bathymetry Data: GEBCO_2020 Grid*. (General Bathymetric Chart of
321 the Oceans, Accessed 20 January 2022).

322

323 [11] Borrero, J. C., Goring, D. G., Greer, S. D., & Power, W. L. Far-field tsunami hazard in New
324 Zealand ports. *Pure and Applied Geophysics*, 172(3), 731-756. (2015)

325

326 [12] Borrero, J.C., Solihuddin, T., Fritz, H., Lynett, P., Prasetya G. et al. Field Survey and
327 Numerical Modeling of the November 22, 2018 Anak Krakatau Tsunami. *Pure and Applied*
328 *Geophysics*, 177, 2457-2475 (2020).

329

330 [13] Gilmour, A.E. Response of Wellington Harbour to the tsunamis of 1960 and 1964. *N. Z. J.*
331 *Mar. Fresh. Res*, 24, 229-231 (1990).

332

333 [14] Patton, J., Graehl, N., Bott J., & Wilson, R. Tsunami response and impacts from the 15
334 January, 2022, tsunami generated by the Hunga Tonga-Hunga Ha’apai volcanic eruption;
335 California Geological Survey Special Report ((2022) [currently in internal agency review,
336 expected publication by 3/11/22]

337

338 [15] La Selle, M., Snyder, A., Nasr, B., Jaffe, B., Ritchie, A., Graehl, N., & Bott J. Observations
339 of tsunami and runup heights in Santa Cruz Harbor and surrounding beaches from the 2022
340 Hunga Tonga-Hunga Ha'apai tsunami. USGS Technical Report: doi:10.5066/P9ZVAB8D.
341 (2022) [currently in internal agency review, expected publication by 3/11/22]

342

343 [16] INDECI. 2022. “Inician acciones de respuesta luego de oleajes en el litoral [Press release,
344 [https://www.gob.pe/institucion/indeci/noticias/576687-inician-acciones-de-respuesta-luego-de-](https://www.gob.pe/institucion/indeci/noticias/576687-inician-acciones-de-respuesta-luego-de-oleajes-en-el-litoral)
345 [oleajes-en-el-litoral](https://www.gob.pe/institucion/indeci/noticias/576687-inician-acciones-de-respuesta-luego-de-oleajes-en-el-litoral)].” NOTA DE PRENSA N 027-2022 COEN INDECI. January 16, 2022.

346

347 [17] UNOCHA. 2022. “PERU: OIL SPILL.” Flash Update 2.

348 [<https://reliefweb.int/report/peru/peru-oil-spill-flash-update-no-02-27-january-2022>] United
349 Nations Office for the Coordination of Humanitarian Affairs (OCHA).

350

351 [18] Medici, E. F., Allen, J. S., & Waite, G. P. Modeling shock waves generated by explosive
352 volcanic eruptions. *Geophysical Research Letters*, 41(2), 414-421. (2014)

353

354 [19] Yokoo, A., Ichihara, M., Goto, A., & Taniguchi, H. Atmospheric pressure waves in the field
355 of volcanology. *Shock Waves*, 15(5), 295-300. (2006)

356

357 [20] Fitzgerald, T. J. Observations of total electron content perturbations on GPS signals caused
358 by a ground level explosion. *Journal of Atmospheric and Solar-Terrestrial Physics*, 59(7), 829-
359 834 (1997).

360

361 [21] Kim, D. H., Lynett, P. J., & Socolofsky, S. A. A depth-integrated model for weakly
362 dispersive, turbulent, and rotational fluid flows. *Ocean Modelling*, 27(3-4), 198-214. (2009).

363

364 [22] Monserrat, S., Vilibić, I., & Rabinovich, A. B. Meteotsunamis: atmospherically induced
365 destructive ocean waves in the tsunami frequency band. *Natural hazards and earth system
366 sciences*, 6(6), 1035-1051. (2006).

367

368 [23] Proudman, J. The effects on the sea of changes in atmospheric pressure, *Geophys. Suppl.*
369 *Mon. Notices R. Astron. Soc.*, 2(4), 197– 209. (1929)

370

371

372 **Methods**

373 *Water Level Time Series Processing and Spectral Analyses*

374 The New Zealand tide gauge data was obtained from the GeoNet program of New Zealand's
375 Institute of Geological and Nuclear Science (GNS). The GeoNet stations are referred to by a four-
376 letter code such as "AUCT" for Auckland. We downloaded the 1-Hz "LTT" dataset which is
377 provided with the tide signal removed from a publicly accessible FTP server. We then processed
378 the 1-Hz data by despiking using the *rmoutliers* function in Matlab which removed any outliers
379 more than 4 standard deviations from the mean of a 100-element moving window. A low pass
380 filter was applied to remove any noise below 0.5 Hz. A subsequent high pass filter was applied
381 with a cut-off of 4.16 hours to remove any residual tidal components. The timeseries were binned
382 to subsample the signal to a 15 second sampling rate (consistent with the DART data described
383 below).

384 Deep-water tsunami data were obtained from NOAA's array of DART tsunameters deployed
385 throughout the Pacific Ocean and from the New Zealand DART array. When in normal operation
386 DART gauges sample every 15-minutes but when they are triggered, on detection of an event, the
387 sampling rate is increased to 15 seconds. Only 15 second data was used in this analysis. The data
388 were despiked removing points more than 2.3 standard deviations from the mean of a 50-element
389 moving window. A subsequent high pass filter was applied with a cut-off of 4.16 hours to remove
390 any residual tidal components.

391 The Continuous Wavelet Transform (CWT) follows the evolution of the frequency content of the
392 sea level records over the duration of the tsunami events. It performs a similar function as short-
393 term Fourier transform (STFT) in that it can be used to analyze time series that contain

394 nonstationary power at many different frequencies, as is the case here where dominant observed
395 frequencies are dependent on the interaction between the incoming tsunami and the resonant
396 frequencies of the receiving environment. The method used here follows that described by [1].
397 Wavelet analysis was carried out using a Morlet wavelet, as it is complex and therefore useful for
398 identifying changes in frequency components over time. It is also a wavelet which has moderate
399 width in both the time and frequency domain, allowing for reasonable resolution in both
400 dimensions [1]. The results of this analysis produce highly redundant but informative spectrograms
401 of the sea level time series.

402 Example timeseries plots of the GeoNet and DART data are shown in Extended Data Figure 1, for
403 the Wellington Harbor tide station and the NZG DART sensor. The Wellington Harbor data is an
404 excellent example of the persistence of this event, with tsunami impacts observed in the harbor for
405 more than 30 hours after the arrival of the initial waves. The CWT also clearly shows the energy
406 banding in the resonance modes of the harbor. The NZG DART is the closest deep-water sensor
407 to the source. From the CWT, the arrival of the leading waves, with periods between 10 and 40
408 minutes, is followed by a packet of much shorter wave energy, with periods less than 5 minutes.

409

410 *Pressure Time Series Processing*

411 The 134 unique pressure time series were sourced from the following authorities. All pressures
412 from the United States were collected from the National Oceanic and Atmospheric Association's
413 (NOAA) National Data Buoy Center and were sampled at 6-minute [2]. Data from Japan was
414 collected from the Japan Meteorological Agency and had 10-minute sampling [3]. Fiji pressure
415 data was collected from the Fiji Meteorological Service and was sampled at 10 minutes [4]. Tonga

416 data was collected from the Nomuka and Nuku'alofa All Weather Stations and was sampled every
417 10 minutes. All pressure time series were collected starting on 15 January at 00:00 UTC until 16
418 January 23:59 UTC.

419 Distances from the explosion were calculated as Euclidean “as the crow flies” distance in km from
420 the weather station to the location of Hunga Tonga island, [-20.536000, -175.382000], utilizing
421 the Haversine equation implemented in Python, which assumes a spherical earth and ignores
422 ellipsoid effects. Distances were calculated in km rounded to the nearest tenth of a meter.

423 Pressure was first normalized to the first pressure reading of the time series, to capture change in
424 pressure in contrast to background pressure, therefore standardizing comparisons across pressure
425 gauges. Each time series was high-pass filtered utilizing the Matlab built-in *highpass* function,
426 with a steepness coefficient of 0.99, defining the transition width of the filter as 0.01 times the
427 stopband frequency. For all of the time series, the stopband frequency was set at $1/2e4$ Hz, or
428 approximately $\frac{1}{5}$ hour⁻¹. The filtered signal demonstrated the pressure pulse uncoupled with
429 standard fluctuations in atmospheric pressure at each gauge. Subsequently, the pressure time series
430 was interpolated onto a 10-second time grid over the 48-hour sampling period utilizing cubic spline
431 interpolation, with the time of explosion (04:15 UTC) as the reference time.

432 The leading pressure pulse was determined by creating a user-defined search window +/- 1 hour
433 from the estimated time of arrival. For example, the Fiji pressure data search window was [1 3],
434 as the pressure pulses on Fiji arrived approximately 2 hours after the eruption. Once the leading
435 pressure pulse was established, the Matlab built-in minimum and maximum functions were utilized
436 to determine the amplitude of the leading pressure pulse and subsequent trough, as well as the
437 corresponding time of arrival for each value and pulse duration. The duration of the positive

438 leading pulse is defined as the time between the pressure reading at 0.2 of the maximum pressure.
439 For each time series, the following values were recorded: pulse and trough amplitude normalized
440 to individual pressure gauge, pulse and trough arrival time in seconds since explosion, and pulse
441 duration in seconds.

442

443 *Air-Pressure Pulse Model*

444 To capture the propagation of the air-pressure pulse across the Pacific Ocean, we develop an
445 empirical pressure pulse evolution model. The general form of the air-pressure N-wave model is:

$$446 \quad P(r, t) = p_{crest} * e^{-\theta_{crest}} - p_{trough} * e^{-\theta_{trough}}$$

447 where

448 P is the time and space-varying function of the air pressure (Pa),

449 t is the time post-eruption (s),

450 r is the distance from the volcano source (m),

451 p_{crest} is the time-dependent amplitude of the leading pressure crest (Pa),

452 p_{trough} is the time-dependent amplitude of the trailing pressure trough (Pa),

453 θ_{crest} is the square of the time- and space-dependent phase function of the pressure crest,

454 and

455 θ_{trough} is the square of the time- and space-dependent phase function of the pressure
456 trough.

457 To determine the empirical relationship for the crest and trough amplitude, we perform a statistical
458 analysis on the 134 weather station pressure observations throughout the globe. For each
459 observation, we determined the crest amplitude, trough amplitude, crest arrival time, and trough
460 arrival time. Through minimizing the error between observation and empirical fit, we find the
461 following relations:

$$462 \quad c_{crest} = 305 * \tanh \left[\frac{t + 300}{4000} \right]$$

$$463 \quad c_{trough} = 295 * \tanh \left[\frac{t}{7000} \right]$$

$$464 \quad p_{crest} = \frac{2.2 * 10^6}{2\pi R_c^{0.5}} * \tanh \left[\frac{R_c}{3.0 * 10^5} \right]^2$$

$$465 \quad p_{trough} = \frac{8.0 * 10^8}{2\pi(R_t + 2.0 * 10^5)^{0.9}}$$

466 where:

467 c_{crest} is the time-averaged wave speed of the crest at time t [m/s],

468 c_{trough} is the time-averaged wave speed of the trough at time t [m/s],

469 $R_c = c_{crest} * t$, is the radial distance the crest has traveled at time t [m], and

470 $R_t = c_{trough} * t$, is the radial distance the trough has traveled at time t [m].

471 These trends, as well as the observed data, are shown in Extended Data Figure 2. We remark that
472 the crest pressure expression includes the *tanh* function, which acts to reduce the amplitude of the
473 positive pressure pulse near to the source. This is a required modification and is indicated by the
474 pressure data measured in Tonga and Fiji.

475 With these data-fitted trends, the square of the phase function is given as $\theta_{crest} = \left(\frac{r-R_c}{0.75*L_c}\right)^2$ and
476 $\theta_{trough} = \left(\frac{r-R_t}{0.75*L_t}\right)^2$, where L_c and L_t are the time-dependent length scales of the crest and trough,
477 respectively. These length scales are calculated as the product of the speed and period of the crest
478 and trough. Here, we attempted to determine the period of these pulses using a statistical analysis
479 of the time series but found that the scatter in these observed periods was extremely large, due
480 mainly to the transient nature of the pressure pulse and noise in the pressure observations at similar
481 periods as the pulse. Thus, we use the data trends as a guidance, but tune the period calculations
482 based on an error minimization between the predicted pressure time series and the observed
483 pressure time series at the 134 locations. Using this procedure, we find that

$$484 \quad T_{crest} = 2300 * t^{-0.1}$$

$$485 \quad T_{trough} = 3300 * t^{-0.1}$$

486 where both terms have units of seconds. With this pressure pulse model, we can recreate the
487 average behavior of the pulse throughout the Pacific, away from the immediate near field. Various
488 model-data comparisons are given in Extended Data Figure 3. The pressure waveform is accurately
489 captured by the model, including at the nearfield stations. As evident from the New Zealand
490 observations, topography and local weather can play a second-order role in modifying the shape
491 and arrival time of the waveform. In the far field, including stations in Japan and the USA, model

492 data agreement is still high, however the pressure pulse signal begins to approach the natural noise,
493 or local pressure fluctuations. Therefore, clearly identifying the air-pressure pulse becomes
494 increasingly difficult.

495

496 *Boussinesq Water Wave Model*

497 The tsunami propagation is simulated using the Boussinesq-type equations, which are a depth-
498 integrated form of the Navier-Stokes equations, valid for weakly dispersive and strongly nonlinear
499 waves [5]. The Boussinesq-type model incurs a significant computational cost in comparison to
500 the Shallow Water Wave Equations traditionally used for tsunami predictions. However, as
501 indicated by the high-frequency energy observed in the DART stations in the range of 3-5 minutes,
502 we expect that dispersion may play an important role in this event. The air-pressure pulse is
503 coupled with the tsunami through a gradient forcing term in the momentum equations [6]. Thus,
504 the air-pressure pulse can contribute energy to the ocean but not the reciprocal, as the empirical
505 form of the air-pressure model implicitly includes the ocean coupling that occurred during the
506 event.

507 Simulations are performed on three different nested grids. The first grid, or local grid, is centered
508 on the volcano, and includes the islands in the immediate vicinity of the volcano. The dimensions
509 of this grid are 170 km by 200 km, with a constant grid resolution of 100 m. Simulations in this
510 grid provide the tide station comparison shown in Figure 4.

511 The second grid, or South Pacific grid, includes Fiji and New Zealand, with coverage from 45°S
512 to 0° latitude and -160° to -180° longitude. A constant grid resolution of 1 km is used for this
513 domain. Simulations in this grid provide the New Zealand DART comparisons shown in Figure 4.

514 The third grid is the Pacific-wide grid, with coverage from 80°S to 80°N latitude and -160° to 120°
515 longitude. A constant grid resolution of 3 km is used for this domain. Simulations in this grid
516 provide the USA NOAA DART comparisons shown in Figure 4.

517 For the local grid, bathymetry and topography are both sourced from a high-resolution data set that
518 integrates The General Bathymetric Chart of the Oceans (GEBCO), nautical charts, LiDAR
519 topography, multibeam bathymetry data, other offshore surveys, and hand-digitized data. The
520 bathymetry was compiled as part of a Multi-Hazard Assessment project sponsored by the Asian
521 Development Bank [7, 8]. For the South Pacific and Pacific-wide grids, the GEBCO 15-s (2021)
522 dataset is used. The data from these sources is bi-linearly interpolated to fit the numerical grid.

523

524 *Crater Collapse Source*

525 For the crater collapse source, we employ a simple radial Gaussian initial condition of the form

$$526 \quad A * e^{-(r/w)^2}$$

527 where A is the initial amplitude of the impulse and W is the characteristic length. The simulations
528 presented in this paper use an amplitude of -100 m and a length of 2 km. These values were
529 primarily chosen based on agreement with observational data but are also representative of the
530 length scales of the volcano. We remark that one could perform extensive tuning with a set of

531 Gaussian units sources to achieve better agreement at the Nuku’alofa tide gage. We choose not to
532 include such an analysis here, as a complex application of a simple, idealized source is not justified.

533

534 *Shockwave Source*

535 The pressure from the early-time shockwave is modeled following [9]. The model provides a time
536 and space varying pressure shockfront, which is included in the hydrodynamic model in the same
537 way as the air-pressure pulse model. The shockwave model calculations are primarily dependent
538 on specification of the energy released by the explosion, which at the time of this writing is
539 uncertain. We assume an energy release of 1.0×10^{16} J, which does create a significant (>10m)
540 tsunami near the source but is secondary to the water-crater source in the nearfield, and
541 insignificant in the far-field.

542

543 *Model Simulations*

544 All simulations approximate bottom friction by a quadratic friction drag law, with a friction
545 coefficient of 0.005. No other dissipation models are used with these simulations. Simulations are
546 run on a large computer cluster. The local grid was run on 400 cores and required 10 hours of wall
547 clock compute time. The South Pacific and Pacific-wide grids were run on 1000 cores, and
548 required 10 and 24 wall clock hours, respectively.

549 Model comparisons with all Pacific DART stations are shown in Extended Data Figure 4. We note
550 that six of these comparisons are shown in Figure 4 in the paper. The model captures the arrival

551 time, amplitude, and in the majority of comparisons, the multi-frequency train of waves.
552 Furthermore, we include four additional model comparisons at tide stations in the South Pacific,
553 provided in Extended Data Figure 5. As the South Pacific grid uses a 1 km grid spacing, coastal
554 amplification effects are missing in the model results. Therefore, we have chosen locations that
555 are reasonably represented in the GEBCO database and exist on relatively simple coastlines. We
556 note that the data sampling frequency at the Niuatoputapu tide gauge is 5 minutes, and thus this
557 signal is unable to resolve the 3 to 5-minute periods found in the model results. Model data
558 agreement is high in the locations which use a 1 minute sampling rate.

559 **Methods References**

560 [1] Torrence, C. & Compo, .P. A Practical Guide to Wavelet Analysis. *Bulletin of the American*
561 *Meteorological Society* 79, 61-78 (1998).

562

563 [2] NOAA. *Meteorological Stations, NOAA Tides and Currents*. (National Oceanic and
564 Atmospheric Administration, Accessed 20 January 2022).

565

566 [3] Japan Meteorological Agency. *Ocean Data Buoy Observations*. (Accessed 20 January 2022).

567

568 [4] Fiji Meteorological Service. (Accessed via Data Request).

569

570 [5] Kim, D. H., Lynett, P. J., & Socolofsky, S. A. A depth-integrated model for weakly
571 dispersive, turbulent, and rotational fluid flows. *Ocean Modelling*, 27(3-4), 198-214. (2009).

572

573 [6] Vilibić, I., Monserrat, S., Rabinovich, A., & Mihanović, H. Numerical modelling of the
574 destructive meteotsunami of 15 June, 2006 on the coast of the Balearic Islands. *Pure and Applied*
575 *geophysics*, 165(11), 2169-2195. (2008).

576

577 [7] ADB. Regional: Pacific Disaster Resilience Program, Multi-Hazard Risk Assessment,
578 Tongatapu Technical Risk Assessment, Report prepared by Arup Australia for Asian
579 Development Bank Project 50028-001. (2021)

580

581 [8] Borrero, J., Greer, D., McIntosh, R., & Damlamian, H. Tsunami Hazard Assessment for
582 Tongatapu, Tonga. *Proceedings Australasian Coasts & Ports 2021 Conference*. (2021).

583

584 [9] Dragoni, M., & Santoro, D. A model for the atmospheric shock wave produced by a strong
585 volcanic explosion. *Geophysical Journal International*, 222(2), 735-742. (2020)

586 **Acknowledgments**

587 The University of Southern California (USC) authors were supported by US NSF grants OCE-
588 1830056 and ICER-1940315. Any opinions, findings, and conclusions or recommendations
589 expressed in this material are those of the authors and do not necessarily reflect the views of the
590 National Science Foundation. The team acknowledges the USC Center for Advanced Research
591 Computing for the 0.5 million CPU hours used for this modeling effort.

592

593 **Author Contributions**

594 Lynett was responsible for leading the overall team, developing the N-wave pressure pulse model,
595 and performing the numerical solutions. McCann was responsible for performing the Ventura
596 Harbor field survey, organizing the manuscript, processing, and curating the pressure time series
597 data. Zhou was responsible for performing the Ventura Harbor field survey, collecting
598 observational data, and creating visualizations with the model output. Renteria participated in the
599 Ventura Harbor field survey, and collected and processed the DART and tide station data. Borrero,
600 Greer, Fa'anunu, and Bosserelle collected reports and observations in the near-field, processed

601 New Zealand DART and tide station data, and contributed to the writing of the manuscript. Jaffe,
602 La Selle, Ritchie, Snyder, Nasr, Bolt, and Graehl completed the tsunami field survey of Santa Cruz
603 Harbor and the surrounding areas, and processed the collected data; Jaffe, La Selle, and Ritchie
604 contributed to the writing of the manuscript. Synolakis participated in the delineation of the source
605 mechanisms, and assisted in the writing of the manuscript. Ebrahimi and Cinar participated in the
606 Ventura Harbor field survey, and assisted in the writing of the manuscript.

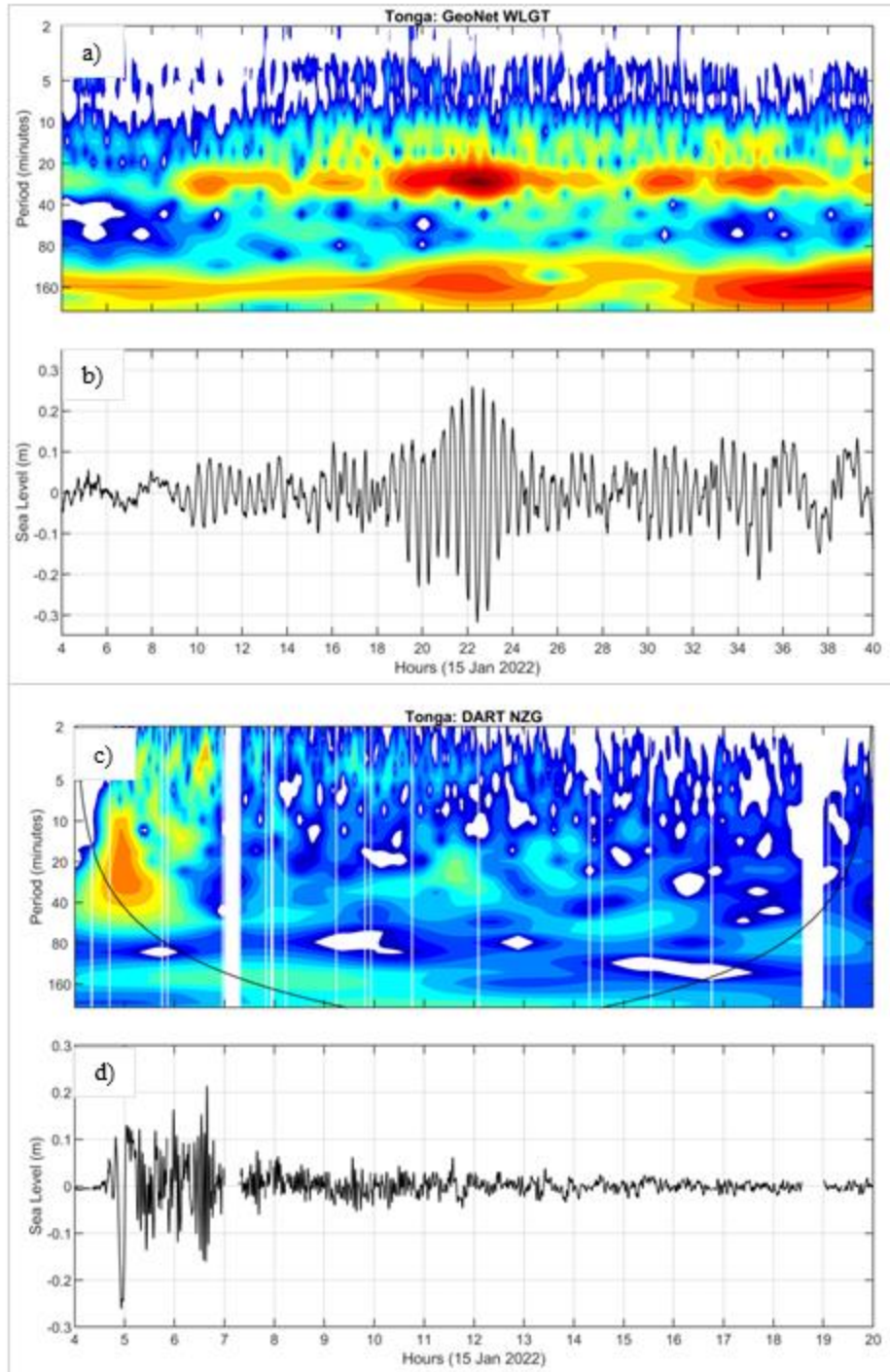
607 **Data Availability**

608 A minimum dataset is provided to demonstrate time series preprocessing methods. A full dataset
609 is available upon request.

610 **Code Availability**

611 Code is presently hosted in a private repository and can be publicly available in a DOI- minting
612 repository upon publication.

613

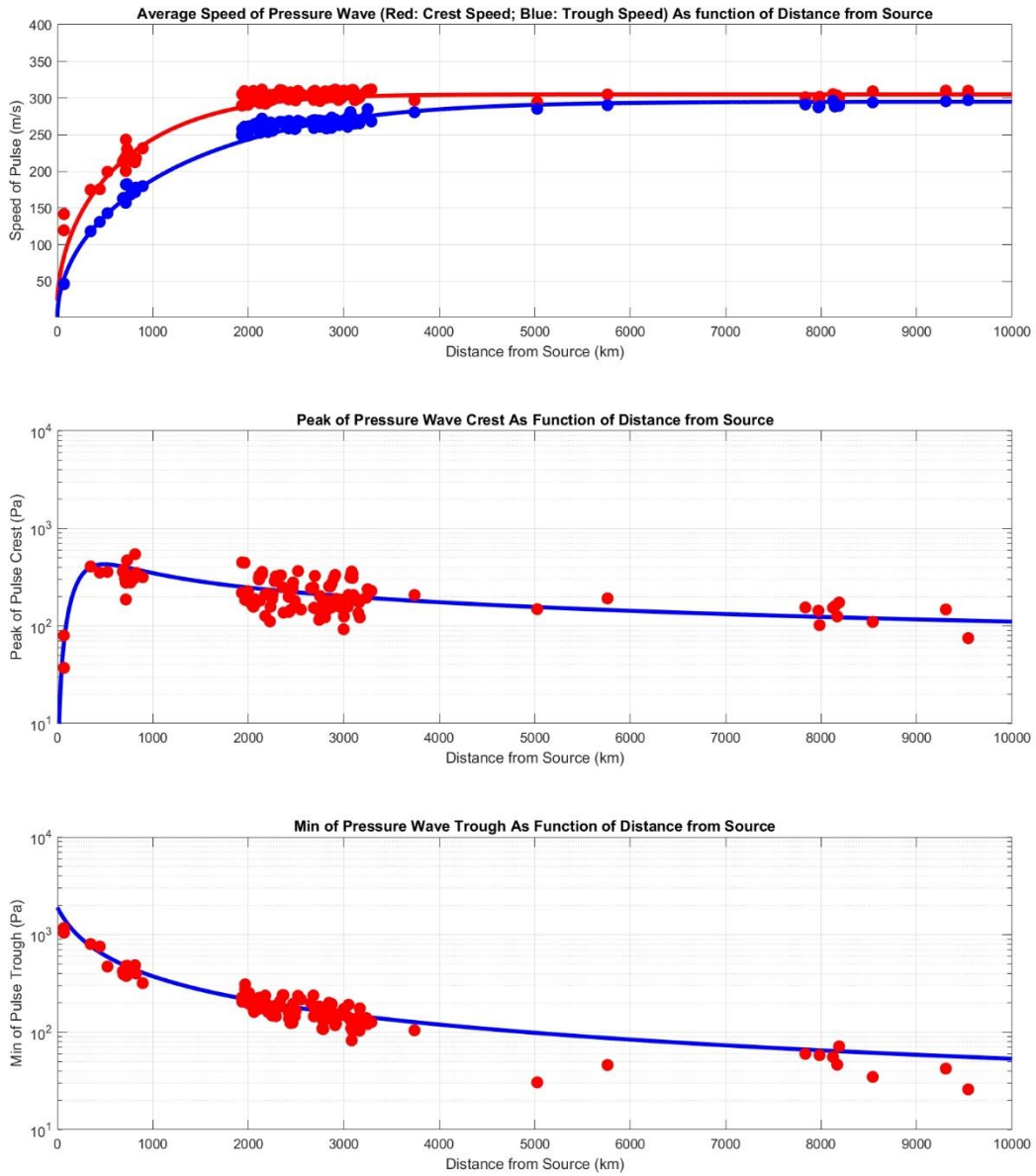


614

615 Extended Data Figure 1. Wavelet analysis and filtered time series data for Wellington Harbor, a)

616 and b); Wavelet analysis and filtered time series data for DART NZG, c) and d).

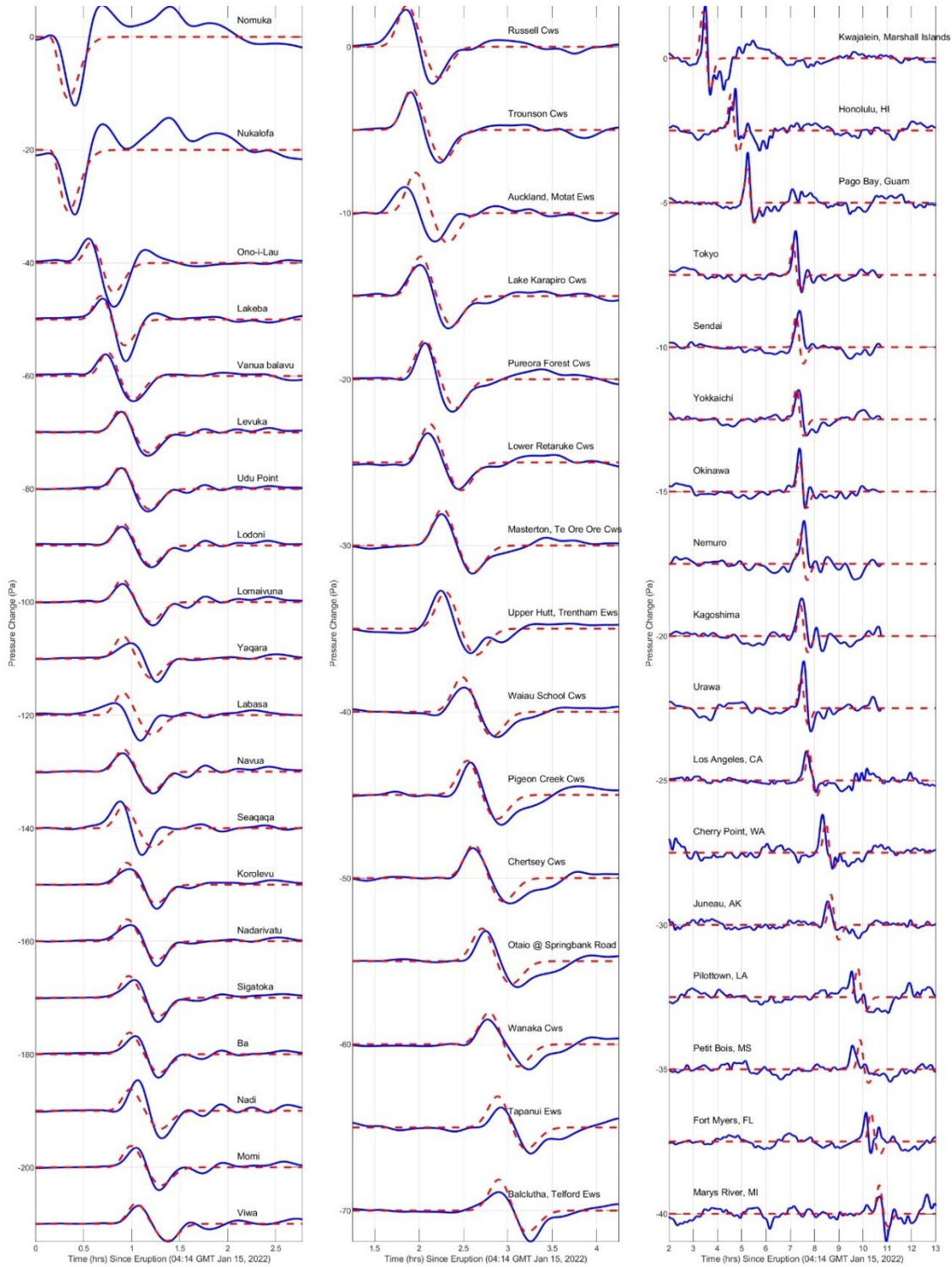
617



618

619 Extended Data Figure 2. Bulk calibration curve fits for the N-wave pressure pulse model; Top:
 620 data (dots) and curve fit (lines) for time-averaged speed of the crest (red) and trough (blue),
 621 assuming a generation time of 04:15 UTC; Middle: data (dots) and curve fit (lines) for crest
 622 amplitude; Bottom: data (dots) and curve fit (lines) for trough amplitude.

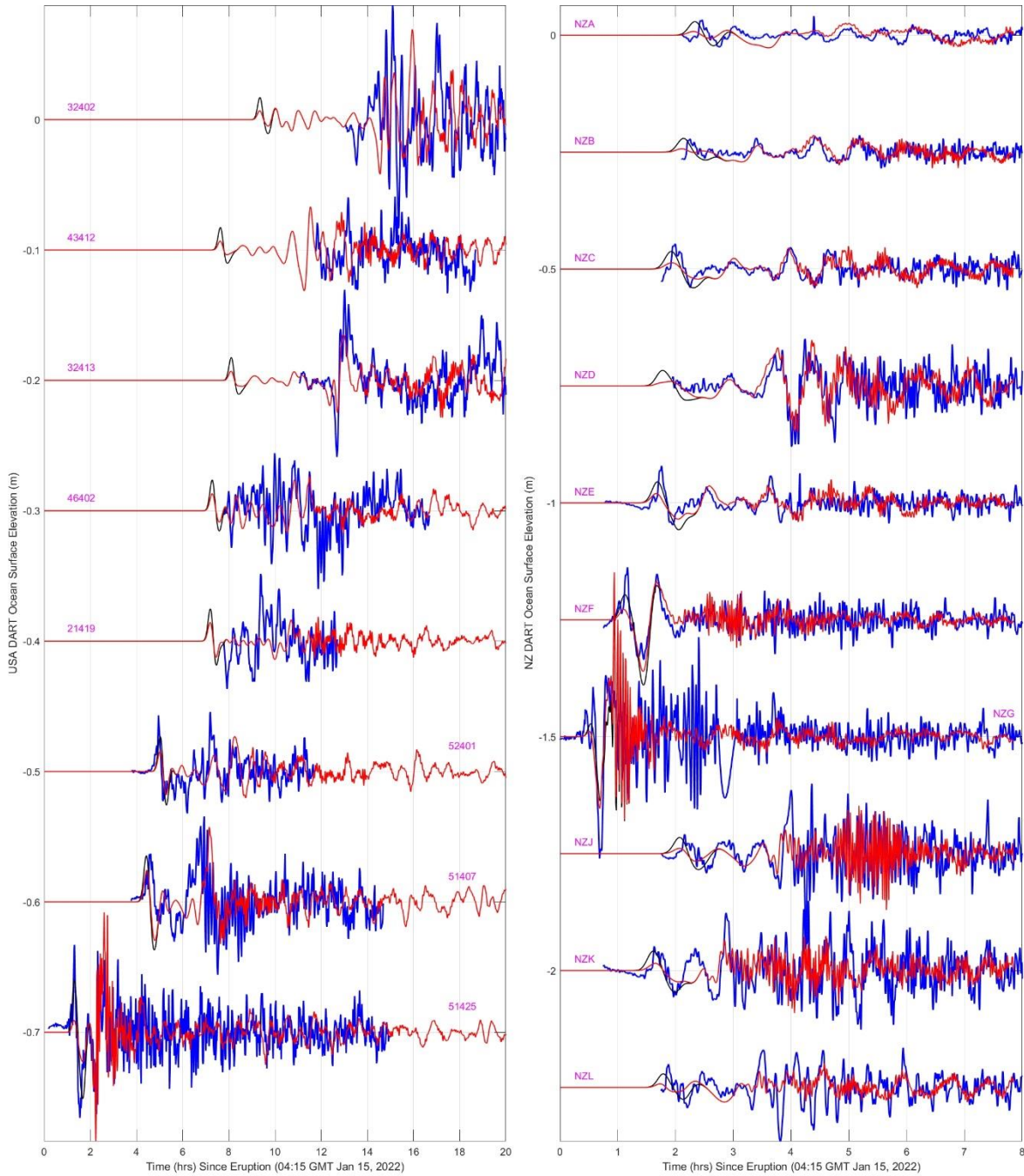
623



624

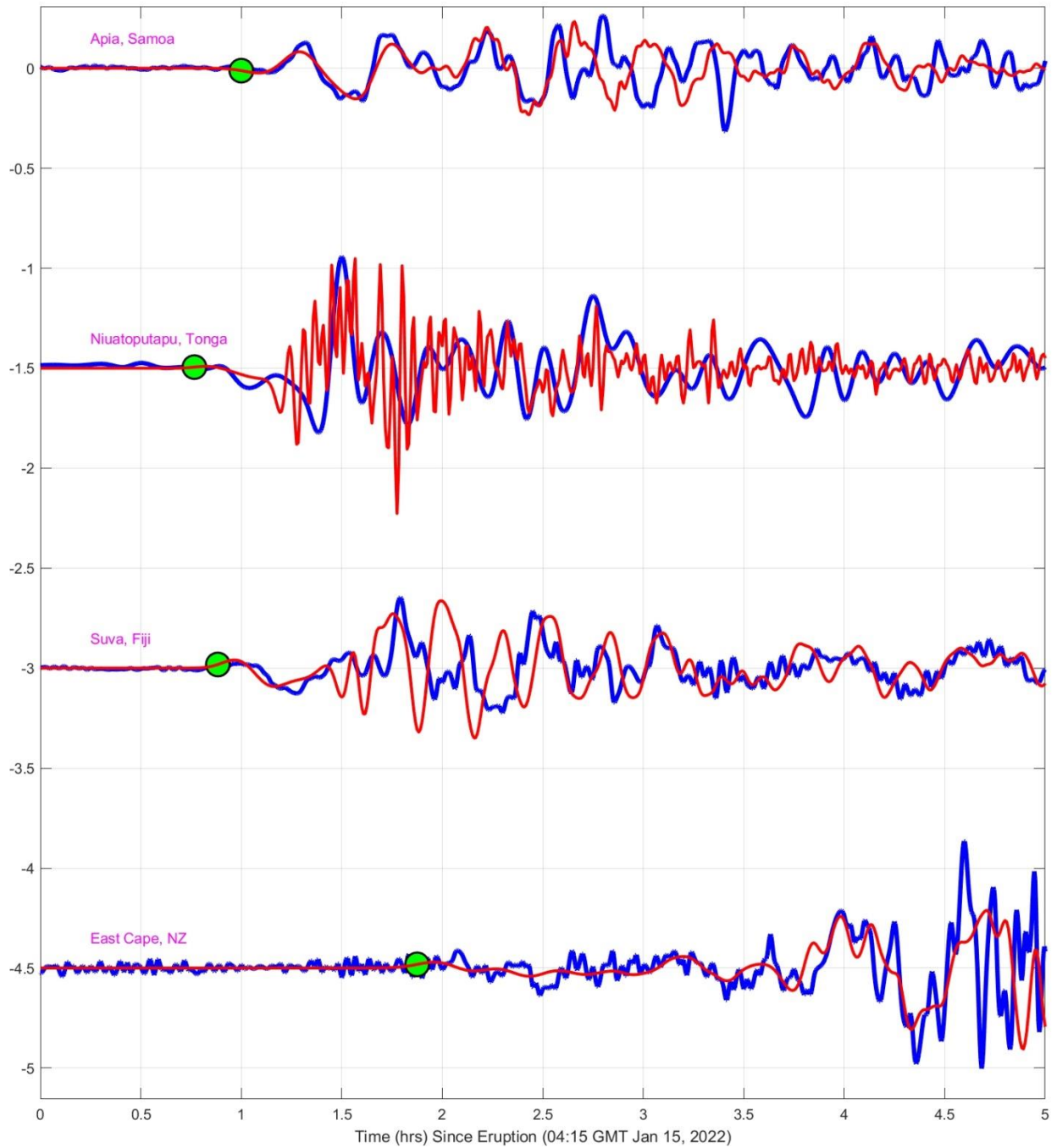
625 Extended Data Figure 3. Summary of pressure time series comparisons with filtered observed data

626 (blue line) and model prediction (red dashed line), where comparison location is given by the text.



627

628 Extended Data Figure 4. Summary of ocean surface elevation time series comparisons with
 629 filtered observed DART data (blue line) and model prediction (dashed line), where comparison
 630 location is given by the text.



631

632 Extended Data Figure 5. Summary of ocean surface elevation time series comparisons with
 633 filtered observed tide station data (blue line) and model prediction (dashed line), where comparison
 634 location is given by the text. The green circle denotes the arrival time of the crest of the pressure
 635 pulse.